Article:
Ansari, S.A., Davidson, J.N. and Foster, M.P. (2025) FEA-based optimisation of an inserted-shunt integrated planar transformer for a bidirectional CLLLC resonant converter. IET Power Electronics, 18 (1). e70014. ISSN: 1755-4535

https://doi.org/10.1049/pel2.70014

IET Power Electronics

WILEY

The Institution of Engineering and Technology

ORIGINAL RESEARCH OPEN ACCESS

FEA-Based Optimisation of an Inserted-Shunt Integrated Planar Transformer for a Bidirectional CLLLC Resonant Converter

Sajad A. Ansari | Jonathan N. Davidson | Martin P. Foster

Department of Electronic and Electrical Engineering, University of Sheffield, Sheffield, UK

Correspondence: Jonathan N. Davidson (jonathan.davidson@sheffield.ac.uk)

Received: 18 November 2024 | **Revised:** 23 January 2025 | **Accepted:** 11 February 2025

Funding: Funded by the Engineering and Physical Sciences Research Council under grant EP/S031421/1.

ABSTRACT

This paper presents an optimisation method for an inserted-shunt integrated planar transformer based on 3D simulation in Ansys Maxwell. The optimisation objective is enhanced efficiency and power density for the transformer. Thermal analysis verifies the optimisation to ensure the transformer's operability under limited temperature conditions when its size is reduced. The optimised integrated transformer is implemented for verification, with the presentation of experimental results, including AC resistance, efficiency, operating waveforms, and thermal imagery. Furthermore, the paper provides insight into the loss distribution of the transformer. The study shows that the optimisation enhances the power density of the inserted-shunt integrated planar transformer by 270% compared to the conventional design. Additionally, the CLLLC converter incorporating the optimised transformer achieves approximately 1.84 percentage points higher efficiency than the conventional design.

1 | Introduction

Hard-switched pulse-width-modulated (PWM) converters, such as the boost converter, face limitations when operated at high frequencies under continuous conduction mode (CCM). This is primarily due to increased switching losses at higher frequencies, which, in turn, restrict their efficiency and result in reduced power density. To address this issue, research has explored the integration of soft-switching techniques into hard-switched PWM converters. However, most of these solutions involve the addition of complex auxiliary circuits to the existing topology of the hard-switched PWM converters. This may result in increased complexity and expenses, with no assurance of consistently improved performance [1–3]. Optimisation of the chosen topology is thus necessary to achieve the desired improved performance.

Resonant converters are gradually succeeding conventional hard-switched PWM converters due to their innate soft-switching capabilities, which enable them to deliver high efficiency even at high switching frequencies [4, 5]. Within the various topologies of resonant converters, there is growing interest in the LLC topology, because of its remarkable soft-switching performance, reduced voltage stress on switching devices, and the integration of magnetic components [6–8].

The topology of the LLC resonant converter is presented in Figure 1. Recently, there has been a growing focus on LLC resonant converters for bidirectional power transfer in vehicle-to-grid (V2G) applications [9–11]. To adapt the LLC converter for bidirectional functionality, modifications are required [12]. Specifically, an additional series inductor and capacitor are introduced on the secondary side, as shown in Figure 2a. This modified

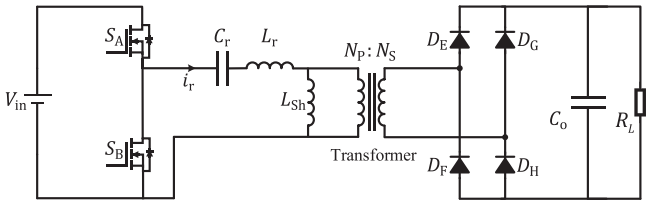

FIGURE 1 | Topology of the half-bridge LLC resonant converter.

topology, which still functions similarly to the LLC configuration, is sometimes referred to as CLLLC converter [13, 14].

As shown in Figures 1 and 2a, both the unidirectional and bidirectional LLC topologies require a high number of magnetic components (three for the unidirectional and four for the bidirectional topology). Magnetic components typically have a significant impact on the cost and size of a converter. Consequently, to enhance the power density and efficiency, the magnetic components of the LLC topologies are commonly integrated into a single magnetic transformer, referred to as an integrated transformer [8, 10, 11]. For example, the magnetic integration for CLLLC topology is presented in Figure 2b. As shown, the primary and secondary leakage inductances of a transformer can be used as the series (or resonant) inductors and the magnetising inductance can be used as the shunt (parallel) inductor of the CLLLC topology.

Magnetic integration has been a significant subject of interest in recent years, resulting in the proposal of numerous methods for magnetic integration in the LLC topology [15–19]. Among these, one of the well-known approaches is the inserted-shunt integrated planar transformer, benefiting from various advantages, such as the accurate estimation of leakage inductance during design, the capability to achieve high leakage inductance, the use of low-cost mass-produced cores and a simple manufacturing process [19–22]. In the integrated transformer which is presented in Figure 3, a magnetically permeable shunt is inserted between two E-cores, with primary and secondary windings positioned on opposite sides of the shunt. The employment of planar E-cores brings additional advantages, such as enhanced power density, improved cooling capabilities, modularity, and a simplified manufacturing process for the transformer.

Inserted-shunt integrated planar transformers were initially developed for use in the unidirectional LLC topology. They share similar characteristics but differ in the topology of their magnetic shunts. These magnetic shunt topologies include low-permeability single-segment shunts [22–24], high-permeability segmental shunts [6, 25] and high-permeability single-segment shunts [26, 27]. In practice, it is preferable to employ high-permeability materials for the shunts due to their broader availability and lower cost. Furthermore, to streamline manufacturing it is advantageous to for shunts to be constructed with a low number of segments.

In a study presented in [28, 29], the magnetic shunt was adapted to make the inserted-shunt integrated transformer compatible with the bidirectional CLLLC converter. This topology can provide asymmetric primary and secondary leakage inductances for the integrated transformer, which is required in the CLLLC converter.

While these inserted-shunt integrated planar transformers have been discussed in the literature, their optimisation has not been thoroughly addressed in the previous research; the previous studies mainly focused on their modelling and ability for magnetic integration. Therefore, there is a lack of optimisation techniques for inserted-shunt integrated transformers in particular in the existing literature.

To address this concern, an optimisation method for the inserted-shunt integrated planar transformer with asymmetric primary and secondary leakage inductances described in [28] is presented in this paper. This topology (in [28]) is chosen because it is suitable for both the unidirectional and bidirectional LLC converters and represents one of the most recent advancements in the inserted-shunt integrated planar transformers. The discussed optimisation method is not only limited to the topology presented in [28], but can also be employed to enhance the performance of other inserted-shunt integrated planar transformers. The proposed optimisation method is based on 3D simulation in Ansys Maxwell and is supported by thermal analysis.

In the literature, optimisation is typically carried out using in-depth mathematical models for winding losses and core losses. Winding losses are commonly calculated using Dowell's model [30]. However, this model cannot be employed to model the winding losses of inserted-shunt integrated planar transformers, as pointed in [31]. Some simplifications can be made to model the winding losses [32, 33]. However, these simplifications still lead to in-depth mathematical model, and they will not guarantee precise estimation. Therefore, it is preferable to estimate the winding losses of inserted-shunt integrated planar transformers using 3D finite-element analysis (FEA) simulations. Consequently, this work utilises 3D FEA simulations for optimisation, eliminating the need for in-depth mathematical analysis. As a result, the presented optimisation procedure is accessible to a wider audience, as it does not require a deep mathematical background, while still providing more accurate results.

The paper is organised as follows: the operation of the inserted-shunt integrated planar transformer with asymmetric primary and secondary leakage inductances is presented briefly in Section 2. In Section 3, the proposed optimisation method is presented. In Section 4, a practical example for optimisation with its simulation study is provided. Experimental results are provided in Section 5 to validate theoretical and simulation results. The conclusion of the work is finally presented in Section 4.

2 | Inserted-Shunt Integrated Planar Transformer With Asymmetric Leakage Inductances

A comprehensive analysis of the inserted-shunt integrated planar transformer, featuring asymmetric primary and secondary leakage inductances, has been covered in [28, 29] and, hence, this paper provides only a brief description of its operation.

The equivalent circuit for a coupled inductor is presented in Figure 4a. This representation can be formally expressed as

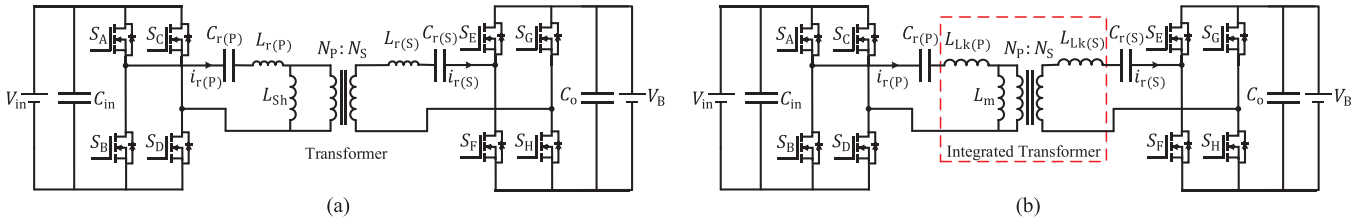

FIGURE 2 | Topology of bidirectional CLLLC resonant converter, (a) without magnetic integration, (b) with magnetic integration.

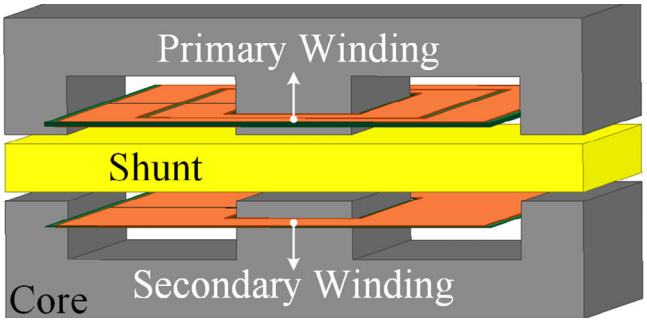

FIGURE 3 | Schematic of the inserted-shunt integrated planar transformer.

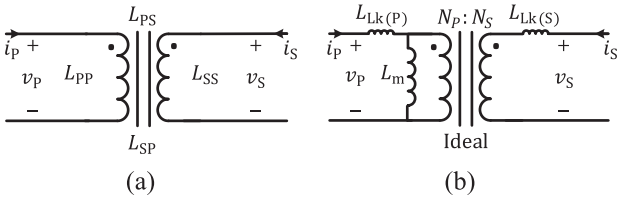

FIGURE 4 | The equivalent circuit of a coupled inductor. (a) First model. (b) Second model.

Equation (1) [18, 34].

$$\begin{bmatrix} v_P \\ v_S \end{bmatrix} = \begin{bmatrix} L_{PP} & L_{PS} \\ L_{SP} & L_{SS} \end{bmatrix} \frac{d}{dt} \begin{bmatrix} i_P \\ i_S \end{bmatrix} \tag{1}$$

where L_{PP} and L_{SS} are primary and secondary self-inductances, respectively, L_{PS} and L_{SP} are mutual inductances and v_P & v_S i_P & i_S are the primary and secondary voltages and currents, respectively.

The coupled inductor can alternatively be depicted using the three-inductor model presented in Figure 4b. This equivalent circuit can be mathematically described as Equation (2). In Equation (2), N_P and N_S are the number of primary and secondary turns, respectively, $L_{Lk(P)}$ and $L_{Lk(S)}$ are primary and secondary leakage inductances, respectively and L_m is magnetising inductance which may be obtained as Equation (3).

$$\begin{bmatrix} v_P \\ v_S \end{bmatrix} = \begin{bmatrix} L_{Lk(P)} + L_m & \frac{N_S}{N_P} L_m \\ \frac{N_S}{N_P} L_m & L_{Lk(S)} + \frac{N_S^2}{N_P^2} L_m \end{bmatrix} \frac{d}{dt} \begin{bmatrix} i_P \\ i_S \end{bmatrix} \tag{2}$$

$$L_m = \frac{N_P}{N_S} L_{PS} \tag{3}$$

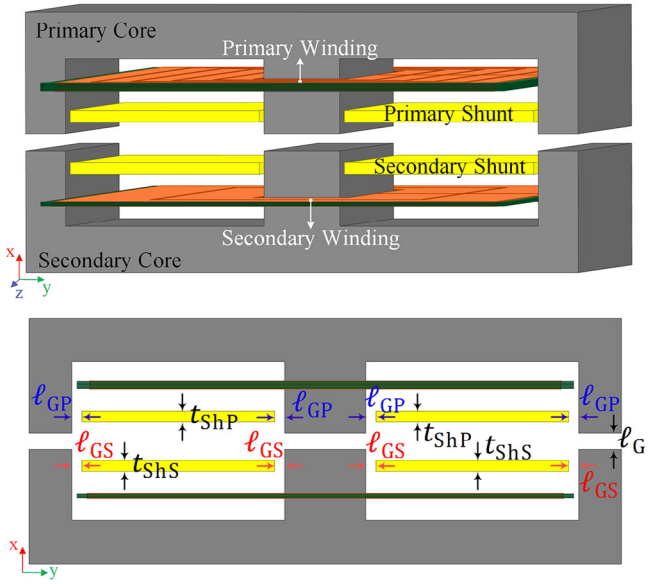

FIGURE 5 | Schematic of the inserted-shunt integrated transformer with asymmetric leakage inductances.

The schematic of the inserted-shunt integrated planar transformer with asymmetric primary and secondary leakage inductance is shown in Figure 5. The structure is divided into primary and secondary sections. The primary section comprises an E-core (primary core), a magnetic shunt (primary shunt), and a winding (primary winding), while the secondary section includes the corresponding secondary elements (secondary core, shunt, and winding). Referring to the equivalent circuit in Figure 4, the operational principles of the transformer are briefly summarised below, with more comprehensive explanations offered in [28, 29].

The primary winding generates a flux in the primary core, which is responsible for producing the primary side inductance (L_{PP} in Figure 4a) of which the magnetising inductance (L_m in Figure 4b) is the largest contributor. A small but significant proportion of the primary flux flows through the primary shunts, which is responsible for the primary side leakage inductance, $L_{Lk(P)}$. Similar arguments lead to the provision of the secondary side leakage inductance ($L_{Lk(S)}$). The remaining component of the primary flux crosses the airgap and couples to the secondary winding and therefore is responsible for the ideal transformer $N_P : N_S$ in Figure 4b.

According to the modelling outlined in [28, 29], the values of the magnetising inductance and the primary and secondary leakage inductances are decoupled from each other. These values can be

obtained from three equations, specifically Equations (17), (29), and (30) of [28]. These equations are expressed in terms of the geometry of the E-cores, windings, and shunts, and also depend on the airgap lengths of the E-cores and shunts. In summary, magnetising inductance is adjusted by regulating the airgap length between the E-cores, ℓ_G. The primary leakage inductance can be adjusted by modifying airgap length, ℓ_{GP}, thickness, t_{ShP} and relative permeability of the primary shunt. Similarly, the secondary leakage inductance is adjusted by altering the airgap length, ℓ_{GS}, thickness, t_{ShS} and relative permeability of the secondary shunt.

3 | Optimisation Procedure

This paper presents a design approach for optimised inserted-shunt integrated planar transformer capable of meeting the specified turns ratio, primary and secondary leakage inductances and magnetising inductance requirements while ensuring high efficiency and reliable operation. Existing literature offers optimisation methods for transformers using mathematical calculations. They often rely on Dowell's 1-D model [30] to calculate the winding losses, assuming uniform magnetic field distribution in both horizontal and vertical directions. However, in the case of LLC resonant converters and inserted-shunt integrated planar transformers, these assumptions no longer hold [31].

For LLC resonant converters, magnetising current should be significant to ensure soft switching, resulting in differing primary and secondary currents (consequently, magnetic field). Moreover, the structure of the inserted-shunt integrated planar transformers can lead to uneven winding and shunt distribution and this introduces non-horizontal magnetic fields. In addition, in the integrated transformers, the presence of airgaps causes significant magnetic flux distribution changes around the windings. The combined effect of these problems is to cause the assumptions required to apply Dowell's method to become invalid. Consequently, to accurately determining the resistance matrix for such designs one should rely on 3D FEA simulations.

FEA is a numerical method used to solve complex physical problems by dividing a system into smaller, simpler parts called finite elements. In this context, 3D FEA simulations are used to model complex electromagnetic interactions with high precision. Tools like Ansys Maxwell apply FEA to solve Maxwell's equations, enabling accurate calculations of parameters such as magnetic flux distribution, eddy currents, and winding/core losses. The software supports customisation of mesh settings, material properties, and boundary conditions, allowing precise modelling of design asymmetries, air gaps, and complex geometries.

In the following section we propose an optimisation approach using 3D FEA simulations to eliminate the need for in-depth mathematical analysis. We then apply this approach to a particular example to demonstrate its utility. This is intended to make the work accessible to a wider audience, as it does not require a deep mathematical background. It is also likely to provide more accurate results at the expense of longer optimisation time. Nevertheless, 3D simulations have become more manageable due to advancements in computer systems, particularly when using the right mesh settings and simulation tools.

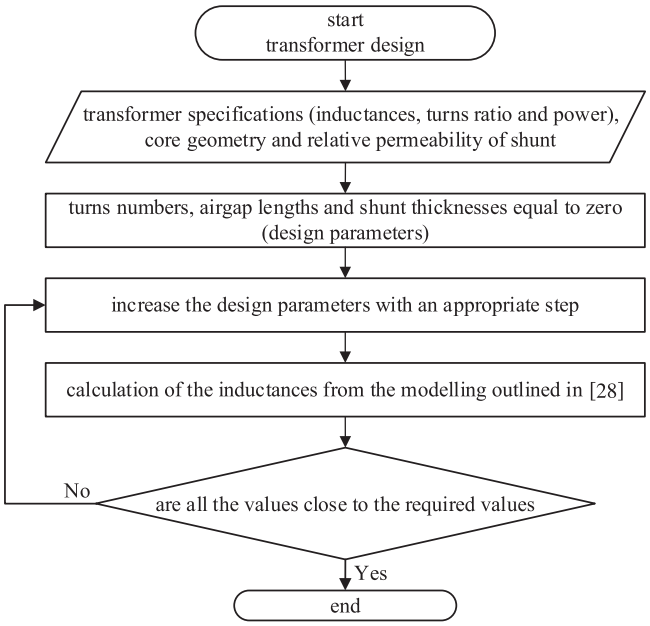

FIGURE 6 | A flowchart for designing the inserted-shunt integrated transformer with asymmetric primary and secondary leakage inductances presented in [28].

To streamline and expedite the simulation process, we make the following considerations:

- *Consideration A*: In accordance with Dowell's 1-D model, in order to reduce the proximity effect, we minimise the number of turns per layer, potentially to one.
- *Consideration B*: We maximise the distance between windings and their corresponding shunts to reduce the effect of fringing (due to the airgaps) on the windings.
- *Consideration C*: We choose a low-permeability shunt, or choose a high-permeability shunt in combination with a distributed air gap, to reduce fringing effect.
- *Consideration D*: We change the parameters (such as the thickness of the PCB trace) to find the optimum efficiency, but the post-design components must be readily available in the market. In other words, we restrict the choice of PCB trace thickness, shunt relative permeability, and the thickness of both the shunt and PCBs to commercially available values in order to ensure the design is realistically manufacturable.
- *Consideration E*: For each inserted-shunt integrated transformer, a specific design procedure is necessary to meet particular requirements, such as primary and secondary leakage inductances, magnetising inductance, and turns ratio. To design an integrated transformer, we employ the modelling technique unique to that transformer type, which is typically detailed in the publication where it was first introduced [6, 19–29]. For example, for the integrated transformer with asymmetric primary and secondary leakage inductances with the modelling presented in [28], we follow the flowchart presented in Figure 6 for the design process. It should be mentioned we have created this flowchart based on the descriptions in [28]. This same flowchart is applicable to other inserted-shunt integrated transformers as well; however, it is

important to reference the specific modelling detailed in their respective papers.

To achieve the most efficient planar core with the smallest footprint, we follow the steps outlined below. These steps will be further illustrated through an example in Section 4.

- *Step 1*: Using a flowchart similar to Figure 6, we select the smallest planar core available in the market that can meet the required specifications of the integrated transformer (primary and secondary leakage inductances, magnetising inductance and turns ratio) without saturating, along with a few larger available planar cores for comparison. For example, in [35], a list of available planar cores manufactured by Magnetics Inc. are presented, which we use.
- *Step 2*: Using a flowchart similar to Figure 6, we design an inserted-shunt integrated transformer that meets the specified requirements (primary and secondary leakage inductances, magnetising inductance and turns ratio) for each core at various flux densities.

  The maximum flux density is chosen in accordance with the core datasheet to avoid saturation. The minimum flux density is based on the maximum number of turns that can fit in the core without requiring a too large air gap (to avoid significant fringing effect) and still achieving the required specifications.

  The flux density in the transformer is adjusted in response to changes in the number of turns in both the primary and secondary windings, with these changes being guided by the turns ratio. For example, in a transformer with a turn ratio of 1:10, an increase of one turn in the primary winding necessitates an increase of ten turns in the secondary winding.

  In the remainder of this paper, when we discuss the different flux densities, it essentially refers to varying numbers of primary and secondary turns.
- *Step 3*: We use 3D simulations and apply considerations A–D, to assess the efficiency (or losses) of each core at various flux densities (turns numbers).
- *Step 4*: We adjust the winding thickness based on market availability to determine the optimal thickness for the windings at each flux density. Essentially, we identify which PCB trace thicknesses are available for purchase and calculate the losses for each thickness using 3D simulation. We then select the thickness that results in the minimum losses. This will help identify the maximum efficiency achievable for each core at each flux density.
- *Step 5*: We compare the optimal design of each core at each flux density, achieved from stage 4, and select the option that offers the highest (or nearly the highest) efficiency while maintaining the smallest size. In other words, if there is an option whose efficiency is close to the highest (the degree of closeness varies with application requirements) but requires a smaller core, we prefer the option with the smaller core. This extra consideration promotes cost-effective manufacturing and simpler cooling.
- *Step 6*: We perform a thermal analysis on the selected core to confirm its operation is within temperature limits. These limits are determined using the core datasheet and the PCB winding datasheet, as the transformer must operate at a temperature that does not compromise the core or the insulation of the windings.

  If the core exceeds the specified temperature threshold, the next larger core with the best achievable efficiency can be selected. Should all cores exceed the temperature limit, we revert to Step 1, selecting larger cores available on the market, and proceed through the subsequent steps anew. This process is repeated until we can design a core that operates within the acceptable temperature range.

TABLE 1 | The bidirectional CLLLC converter's specification.

Symbol	Parameter	Value
$N_P : N_S$	Turns ratio	5:1
L_m	Magnetising inductance	90 μH
$L_{Lk(P)}$	Primary resonant inductance	30 μH
$L_{Lk(S)}$	Secondary resonant inductance	0.8 μH
C_{r1}	Primary resonant capacitance	22 nF
C_{r2}	Secondary resonant capacitance	0.56 μF
V_{in}	Input voltage	125 V
V_{out}	Output voltage	20–26 V
P_{out}	Output power	200 W
f_s	Switching frequency	150-230 kHz

4 | A Design Example

In this section, the optimisation procedure provided in Section 3 is applied on an inserted-shunt integrated planar transformer which needs to be designed for a bidirectional CLLLC resonant converter with the specification outlined in Table 1.

Based on the modelling from [28] and Figure 6, E32-6-20 is the smallest ferrite core that can meet the specification presented in Table 1 without reaching the saturation region. Additionally, three larger ferrite planar cores, E38-8-25, E43-10-28, and E58-11-38, are also selected that can meet the specification presented in Table 1 (step 1). Reference [35] is used to choose the ferrite cores (grade 3F4) with an emphasis on selecting the next three larger cores that do not share a similar volume.

Applying considerations A to E, an integrated transformer with the specification presented in Table 1 is designed for the different cores and at different flux densities, as presented in Table 2, using the modelling presented in [28] and Figure 6 (step 2). It is important to again note that the flux density of a transformer is significantly affected by its number of turns. Therefore, to accommodate different flux densities, the turns number (N_P and N_S) must be adjusted. With the secondary turns set at 1, we get too high flux density, and with more than 4 turns, we encounter too large an airgap. Consequently, three combinations (10:2, 15:3 and 20:4) can only be considered, each resulting in separate flux densities for each core. In addition, the core E-32-6-20 can provide the required specification outlined in Table 1 only when it has winding configuration of 15:3.

TABLE 2 | Characteristics of the designed integrated transformer.

Core	N_P	N_S	ℓ_G	t_{ShP}	t_{ShS}	ℓ_{GP}	ℓ_{GS}
E32-6-20	15	3	0.24 mm	2.15 mm	1.1 mm	0.1 mm	0.1 mm
E38-8-25	10	2	0.14 mm	2.15 mm	1.2 mm	0.1 mm	0.1 mm
E38-8-25	15	3	0.35 mm	0.8 mm	0.4 mm	0.1 mm	0.1 mm
E38-8-25	20	4	0.75 mm	0.35 mm	0.1 mm	0.1 mm	0.1 mm
E43-10-28	10	2	0.17 mm	2.2 mm	1.2 mm	0.1 mm	0.1 mm
E43-10-28	15	3	0.45 mm	0.75 mm	0.35 mm	0.1 mm	0.1 mm
E43-10-28	20	4	0.87 mm	0.3 mm	0.12 mm	0.1 mm	0.1 mm
E58-11-38	10	2	0.23 mm	2.3 mm	1.2 mm	0.1 mm	0.1 mm
E58-11-38	15	3	0.64 mm	0.72 mm	0.34 mm	0.1 mm	0.1 mm
E58-11-38	20	4	1.3 mm	0.3 mm	0.1 mm	0.1 mm	0.1 mm

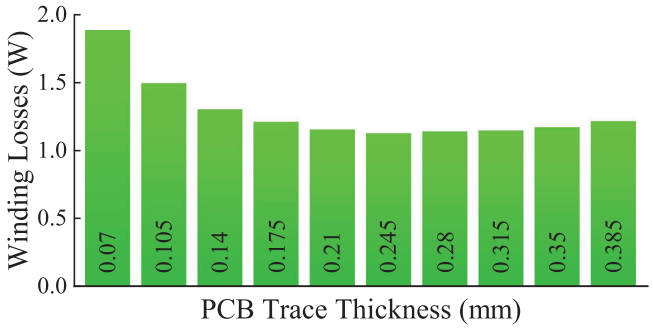

FIGURE 7 | Secondary winding losses at various PCB trace thicknesses.

For each core and at each flux density (turns number), the winding and core losses (for ferrite 3F4) can be estimated using 3D FEA simulation (step 3). To obtain the highest efficiency of each core at each flux density, the thickness of the PCB windings was varied in 0.035 mm increments (a step size available according to [36]) (step 4). For example, the conduction losses of the secondary windings of the core E-38-8-25 with a turn configuration of 15:3 for different thickness of the PCB traces are obtained through 3D simulation with Ansys Maxwell, as presented in Figure 7. The lowest conduction losses can be achieved when the thickness is 0.245 mm. From similar parametric simulations, the optimal thickness of the primary winding was obtained as 0.07 mm. It should be mentioned that the thickness of the PCB traces is limited by both core geometry (it should be able to be fitted) and market PCB availability (it should be possible to be ordered).

Finally, using Ansys Maxwell, the optimum efficiency of each core at each flux density (turns number) is estimated; each is presented in Table 3. The loss distribution of each core at each flux density (turns number) and for the optimal design are presented in Figure 8. As shown, an increase in the number of turns (which reduces the maximum flux density of the core) results in reduced core losses while increasing conduction losses. Typically, the lowest losses for each core are achieved when the winding losses and core losses are roughly equivalent.

According to Table 3, for our specification, the E38-8-25 core with turn number of 15:3 can provide nearly the highest efficiency

TABLE 3 | Efficiency of the optimised integrated transformers.

Core \ Turns number	10:2	15:3	20:4
E32-6-20	–	97.88	–
E38-8-25	98.25	98.62	98.45
E43-10-28	98.31	98.74	98.76
E58-11-38	98.35	98.97	99.07

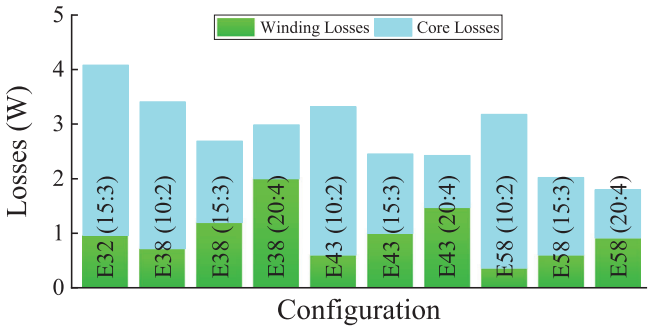

FIGURE 8 | Loss distributions of each configuration.

with the smallest size (step 5). Although the core E58-11-38 with 20:5 turns configuration can provide slightly higher efficiency, it comes at the cost of larger size (almost double).

Using Ansys Maxwell Circuit, the magnetic flux density of the selected design while it operates in a bidirectional CLLLC converter with specification outlined in Table 1 is presented in Figure 9a. As shown, the transformer which is a planar ferrite core does not reach the saturation point. For comparison, Figure 9b presents the magnetic flux density of the original transformer, non-optimised design, as reported in [28]. This original design exhibits a lower flux density due to its larger volume and surface area. However, the goal of an effective design is not merely achieving lower flux density but rather optimising for reduced losses and compact size.

To ensure the reliability of the chosen design, thermal simulations were conducted using a two-way coupling of Ansys Maxwell and

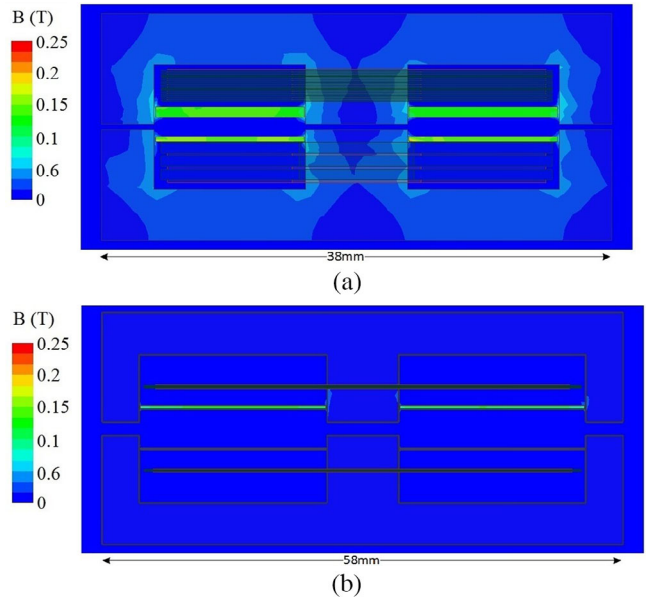

FIGURE 9 | Magnetic flux density. (a) The optimised integrated transformer (core size: 38 mm × 8 mm × 25 mm). (b) The original integrated transformer (core size: 58 mm × 11 mm × 38 mm).

TABLE 4 | Comparison of optimised and original integrated transformers.

Transformer	Core losses (W)	Copper losses (W)	Efficiency (%)	Volume (mm^3)
Optimised	1.55	1.25	98.62	26200
Original	1.05	5.85	96.66	70400

Ansys Icepak. The results are presented in Figure 10a, showing that the core and windings' temperatures remain within acceptable limits. Therefore, this design offers a very high efficiency and a compact size, while still ensuring reliable operation (step 6). For comparison, Figure 10b shows the simulated operating temperature of the original transformer, non-optimised design reported in [28]. The original design shows a lower temperature due to its larger volume and surface area, which result in reduced thermal resistance. However, again, the objective of an effective design is not solely to minimise temperature but to achieve high efficiency and a compact design while ensuring the temperature remains within safe limits.

In Table 4, the losses, efficiency, and volume of both the optimised integrated transformer and the original design are presented. As shown, the optimisation led to higher efficiency and a smaller volume while maintaining the same 200 W output power.

5 | Experimental Verification

To verify theoretical analysis and simulation results, a CLLLC converter using the integrated transformer was implemented as shown in Figure 11a. The integrated transformer is based on the proposed optimised design, with specifications presented in

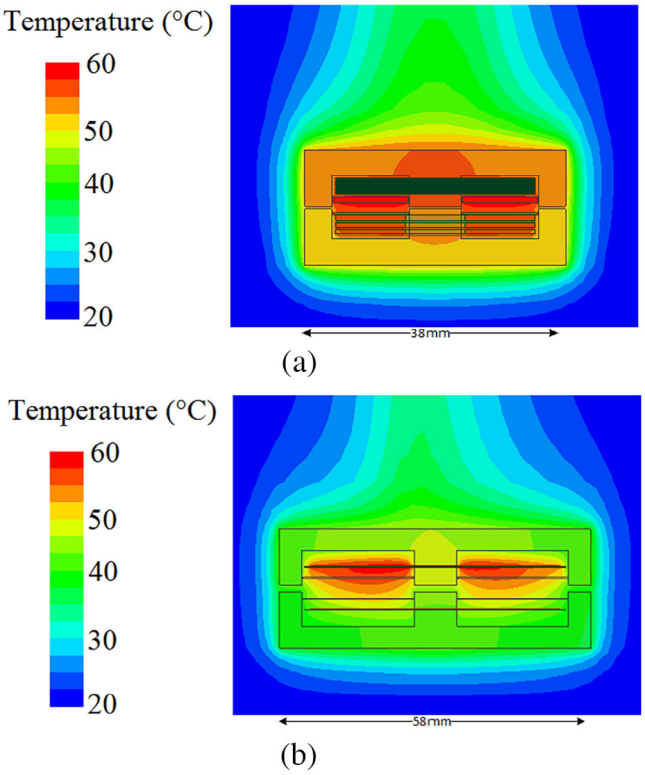

FIGURE 10 | Thermal performance. (a) The optimised integrated transformer (core size: 38 mm × 8 mm × 25 mm). (b) The original integrated transformer (core size: 58 mm × 11 mm × 38 mm).

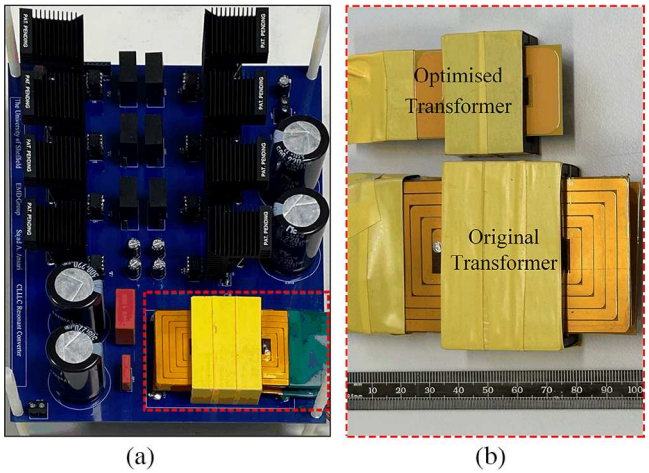

FIGURE 11 | Prototypes. (a) CLLLC converter. (b) The optimised and original integrated transformers.

Table 5, and its prototype is shown in Figure 11b. Furthermore, to demonstrate the effectiveness of the optimisation applied to the topology introduced in [28], the non-optimised integrated transformer (original design) built in [28] (which was constructed using a simple optimisation method proposed in [35]) is compared with the proposed topology, as shown in Figure 11b. Based on the size comparison shown in Figure 11 and considering that both transformers have the same output power, the optimisation resulted in a 270% increase in power density.

TABLE 5 | Optimised structure's parameters.

Symbol	Parameter	Value
N_P	Primary turns	15
N_S	Secondary turns	3
k_P	Turns per layer in primary	1
k_S	Turns per layer in secondary	1
n_P	Number of primary layers	15
n_S	Number of secondary layers	3
h_P, h_S	Primary and secondary conduction thickness	70, 245 µm
$h_{\Delta P}$, $h_{\Delta S}$	Primary and secondary insulation thickness	90, 755 µm
t_{SHP}	Primary shunt thickness	0.8 mm
t_{SHS}	Secondary shunt thickness	0.4 mm
ℓ_G	Transformer air gap	0.37 mm
ℓ_{GP}	Distance between primary shunt and E-core	0.1 mm
ℓ_{GS}	Distance between secondary shunt and E-core	0.1 mm

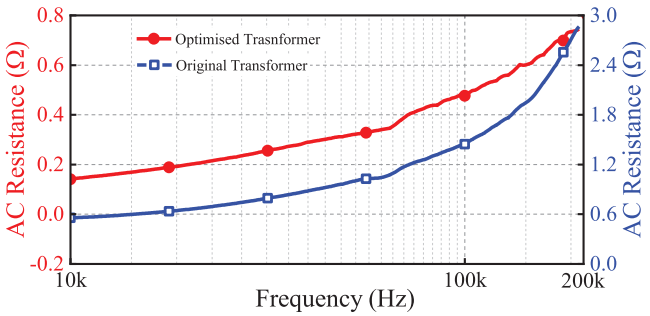

FIGURE 12 | AC resistance of the optimised integrated transformer and the original integrated transformer. Note the different scales left and right.

It should be mentioned that the shunts for these prototypes were easily made by cutting KEMET polymer magnetic shielding sheets (series EFS) and gluing them in parallel to create a stack with the desired thickness.

The AC resistance of the optimised integrated transformer and the original integrated transformer, measured by a frequency analyser Omicron Bode 100, are presented in Figure 12. As shown, the optimisation has reduced the AC resistance of the integrated transformer, resulting in lower conduction losses.

The efficiency of the CLLLC converter using the optimised integrated transformer and the original integrated transformer for different output power levels are presented in Figure 13. As shown, the efficiency has improved by 1.84 percentage

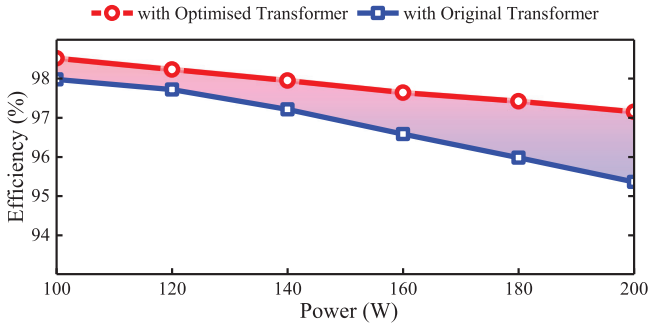

FIGURE 13 | Efficiency of the CLLLC converter without the rectifier stage using the optimised integrated transformer and the original integrated transformer. Power direction from left to right of Figure 2.

points at 200 W output power as a result of the optimisation. The efficiency of the converter is evaluated after removing the rectifier stage from the circuit. Since the losses from an asynchronous rectifier are higher than those in the magnetics, removing the rectifier highlights the efficiency difference between the optimised transformer and the original transformer more effectively.

To confirm the performance of the optimised integrated transformer, the bidirectional CLLLC resonant converter outlined in Table 1 is constructed using the design optimised integrated transformer. Some of the waveforms of the converter in both directions are presented in Figure 14. The converter operates correctly in forward and reverse power transfer modes as illustrated by the gate signal which turns-on after its drain-source voltage has fallen zero, thereby demonstrating zero voltage switching (ZVS) has been achieved.

The thermal image of the optimised integrated transformer is shown in Figure 15a. As shown, the temperature is still within the acceptable range. For comparison, Figure 15b shows the thermal image of original transformer, non-optimised design reported in [28]. As predicted by the simulation results, the original design shows a lower temperature due to its larger volume and surface area, which result in reduced thermal resistance. However, again, the objective of an effective design is not solely to minimise temperature but to achieve high efficiency and a compact design while ensuring the temperature remains within safe limits.

It should be noted that the application of this optimisation method is not limited solely to the inserted-shunt integrated transformer with asymmetric leakage inductances but can be applied to other inserted-shunt integrated transformers. Many inserted-shunt integrated transformers have been recently proposed [6, 19–29], yet their papers do not significant details on design optimisation since they focus mainly on the modelling and operation of the topologies. Nevertheless, optimisation can further highlight the advantages of these topologies. The principal contribution of this work is to demonstrate a robust widely applicable optimisation method for inserted-shunt integrated transformers using FEA simulation tools, which can be utilised by a broad audience of engineers.

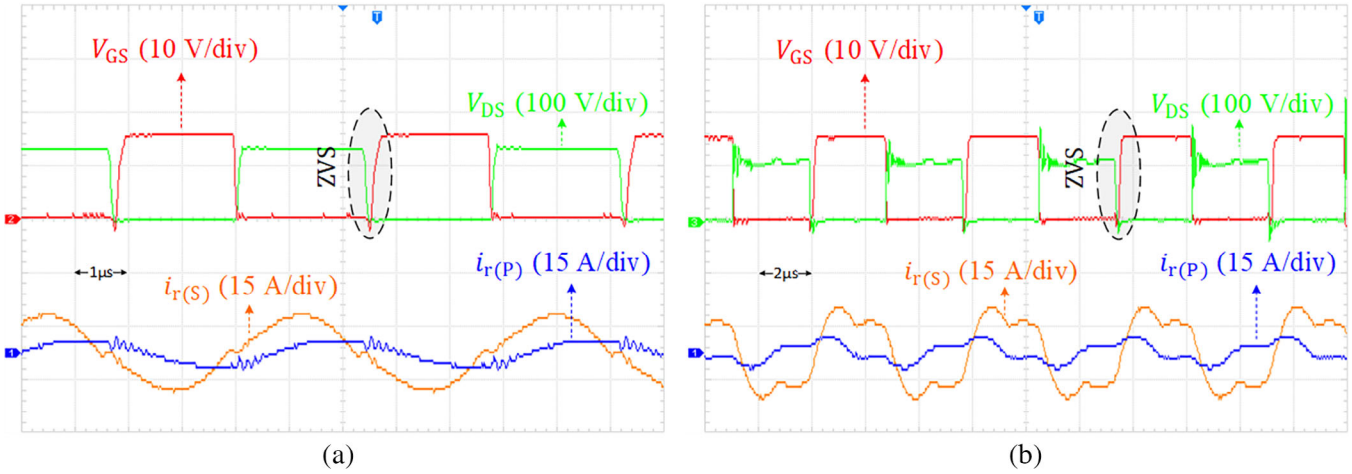

FIGURE 14 | Experimental waveforms of the CLLLC resonant converter using the optimised integrated transformer. (a) In battery charging mode (power direction from left to right of Figure 2). (b) In reverse mode (power direction from right to left of Figure 2). V_{DS} is drain-to-source voltage, V_{GS} is gate-to-source voltage, $i_{r(P)}$ and $i_{r(S)}$ are the primary and secondary resonant currents, respectively (defined in Figure 2).

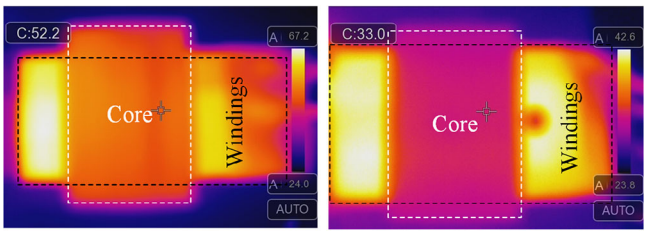

FIGURE 15 | Thermal image of the transformer when it is incorporated within a bidirectional CLLLC resonant converter. (a) The optimised integrated transformer. (b) The original integrated transformer.

6 | Conclusion

In this paper, an optimisation method utilising 3D FEA simulation was presented to enhance the efficiency and power density of the integrated transformers. This method is specifically developed for use with inserted-shunt integrated transformers that cannot be optimised using Dowell's 1-D model. The optimisation technique was applied to a recently introduced inserted-shunt integrated transformer. The results showed that the optimisation enhances the power density of the inserted-shunt integrated planar transformer by 270% compared to the conventional design. Additionally, the CLLLC converter incorporating the optimised transformer achieves approximately 1.84 percentage points higher efficiency than the conventional design. Practical testing of the optimised integrated transformer was conducted by integrating it into a bidirectional CLLLC resonant converter. The experimental results confirm the proper operation of the converter, and thermal image indicates that the optimised integrated transformer remains within an acceptable temperature range.

Author Contributions

Sajad A. Ansari: writing – original draft, writing – review & editing. **Jonathan N. Davidson:** writing – original draft, writing – review & editing. **Martin P. Foster:** writing – original draft, writing – review & editing.

Acknowledgements

This work was supported by the Engineering and Physical Sciences Research Council (EPSRC) under grant EP/S031421/1.

Conflicts of Interest

The authors declare no conflicts of interest.

Data Availability Statement

No data were used for the research described in the article and/or no data are available.

References

1. S. A. Ansari and J. S. Moghani, "A Novel High Voltage Gain Non-coupled Inductor SEPIC Converter," *IEEE Transactions on Industrial Electronics* 66, no. 9 (2018): 7099–7108.

2. S. A. Ansari and J. S. Moghani, "Soft Switching Flyback Inverter for Photovoltaic AC Module Applications," *IET Renewable Power Generation* 13, no. 13 (2019): 2347–2355.

3. S. A. Ansari, J. N. Davidson, and M. P. Foster, "Evaluation of Silicon MOSFETs and GaN HEMTs in Soft-Switched and Hard-Switched DC-DC Boost Converters for Domestic PV Applications," *IET Power Electronics* 14, no. 5 (2021): 1032–1043.

4. J. Deng, S. Li, S. Hu, C. C. Mi, and R. Ma, "Design Methodology of LLC Resonant Converters for Electric Vehicle Battery Chargers," *IEEE Transactions on Vehicular Technology* 63, no. 4 (2013): 1581–1592.

5. S. S. Shah, S. K. Rastogi, and S. Bhattacharya, "Paralleling of LLC Resonant Converters," *IEEE Transactions on Power Electronics* 36, no. 6 (2020): 6276–6287.

6. S. A. Ansari, J. N. Davidson, and M. P. Foster, "Analysis, Design and Modelling of Two Fully-Integrated Transformers With Segmental Magnetic Shunt for LLC Resonant Converters," in IECON 2020 The 46th Annual Conference of the IEEE Industrial Electronics Society (IEEE, 2020), 1273–1278.

7. J. Biela and J. W. Kolar, "Analytic Model Inclusive Transformer for Resonant Converters Based on Extended Fundamental Frequency Analysis for Resonant Converter-design and Optimization," *IEEJ Transactions on Industry Applications* 126, no. 5 (2006): 568–577.

8. Z. Fang, Z. Huang, H. Jing, and F. Liu, "Hybrid Mode-Hopping Modulation for LLC Resonant Converter Achieving High Efficiency and Linear Behaviour," *IET Power Electronics* 13, no. 6 (2020): 1153–1162.

9. W. Chen, P. Rong, and Z. Lu, "Snubberless Bidirectional DC–DC Converter With New CLLC Resonant Tank Featuring Minimized Switching Loss," *IEEE Transactions on Industrial Electronics* 57, no. 9 (2009): 3075–3086.

10. Y. Wei, Q. Luo, and A. Mantooth, "Overview of Modulation Strategies for LLC Resonant Converter," *IEEE Transactions on Power Electronics* 35, no. 10 (2020): 10423–10443.

11. C. W. Tsang, M. P. Foster, D. A. Stone, and D. T. Gladwin, "Analysis and Design of LLC Resonant Converters With Capacitor–Diode Clamp Current Limiting," *IEEE Transactions on Power Electronics* 30, no. 3 (2014): 1345–1355.

12. J.-H. Jung, H.-S. Kim, M.-H. Ryu, and J.-W. Baek, "Design Methodology of Bidirectional CLLC Resonant Converter for High-Frequency Isolation of DC Distribution Systems," *IEEE Transactions on Power Electronics* 28, no. 4 (2012): 1741–1755.

13. Z. U. Zahid, Z. M. Dalala, R. Chen, B. Chen, and J.-S. Lai, "Design of Bidirectional DC–DC Resonant Converter for Vehicle-to-Grid (V2G) Applications," *IEEE Transactions on Transportation Electrification* 1, no. 3 (2015): 232–244.

14. J. Min and M. Ordonez, "Bidirectional Resonant CLLC Charger for Wide Battery Voltage Range: Asymmetric Parameters Methodology," *IEEE Transactions on Power Electronics* 36, no. 6 (2020): 6662–6673.

15. S. A. Ansari, J. N. Davidson, M. P. Foster, and D. A. Stone, "Design and Analysis of a Fully-Integrated Planar Transformer for LCLC Resonant Converters," in 2021 23rd European Conference on Power Electronics and Applications (EPE'21 ECCE Europe) (IEEE, 2021), 1–8.

16. Y. Liu, H. G. Wu, J. Zou, Y. Tai, and Z. Ge, "CLL Resonant Converter With Secondary Side Resonant Inductor and Integrated Magnetics," *IEEE Transactions on Power Electronics* 36, no. 10 (2021): 11316–11325.

17. M. H. Ahmed, A. Nabih, F. C. Lee, and Q. Li, "Low-Loss Integrated Inductor and Transformer Structure and Application in Regulated LLC Converter for 48-V Bus Converter," *IEEE Journal of Emerging and Selected Topics in Power Electronics* 8, no. 1 (2019): 589–600.

18. S. De Simone, C. Adragna, and C. Spini, "Design Guideline for Magnetic Integration in LLC Resonant Converters," in *2008 International Symposium on Power Electronics, Electrical Drives, Automation and Motion* (IEEE, 2008), 950–957.

19. B. Li, Q. Li, and F. C. Lee, "High-Frequency PCB Winding Transformer With Integrated Inductors for a Bi-Directional Resonant Converter," *IEEE Transactions on Power Electronics* 34, no. 7 (2018): 6123–6135.

20. S. A. Ansari, J. Davidson, and M. Foster, "A Design Methodology for a CLLLC Bidirectional Resonant Converter With an Integrated Planar Transformer," in PCIM Europe 2023; International Exhibition and Conference for Power Electronics, Intelligent Motion, Renewable Energy and Energy Management (VDE, 2023), 1–9.

21. S. A. Ansari, "Magnetic Integration Techniques for Resonant Converters," (PhD diss. University of Sheffield, 2023).

22. J. Zhang, Z. Ouyang, M. C. Duffy, M. A. Andersen, and W. G. Hurley, "Leakage Inductance Calculation for Planar Transformers With a Magnetic Shunt," *IEEE Transactions on Industry Applications* 50, no. 6 (2014): 4107–4112.

23. M. Li, Z. Ouyang, B. Zhao, and M. A. Andersen, "Analysis and Modeling of Integrated Magnetics for LLC Resonant Converters," in IECON 2017–43rd Annual Conference of the IEEE Industrial Electronics Society (IEEE, 2017), 834–839.

24. M. Li, Z. Ouyang, and M. A. Andersen, "High-Frequency LLC Resonant Converter With Magnetic Shunt Integrated Planar Transformer," *IEEE Transactions on Power Electronics* 34, no. 3 (2018): 2405–2415.

25. S. A. Ansari, J. Davidson, and M. Foster, "Fully-Integrated Planar Transformer With a Segmental Shunt for LLC Resonant Converters," *IEEE Transactions on Industrial Electronics* 69, no. 9 (2021): 9145–9154.

26. S. A. Ansari, J. N. Davidson, and M. P. Foster, "Fully-Integrated Solid Shunt Planar Transformer for LLC Resonant Converters," *IEEE Open Journal of Power Electronics* 3 (2021): 26–35.

27. S. A. Ansari, J. Davidson, and M. Foster, "Inserted-Shunt Integrated Planar Transformer With Low Secondary Leakage Inductance for LLC Resonant Converters," *IEEE Transactions on Industrial Electronics* 70, no. 3 (2022): 2652–2661.

28. S. A. Ansari, J. N. Davidson, and M. P. Foster, "Fully-Integrated Transformer With Asymmetric Primary and Secondary Leakage Inductances for a Bidirectional Resonant Converter," *IEEE Transactions on Industry Applications* 59 (2023): 3674–3685.

29. S. A. Ansari, J. N. Davidson, and M. P. Foster, "Fully-Integrated Transformer With Asymmetric Leakage Inductances for a Bidirectional Resonant Converter," in 11th International Conference on Power Electronics, Machines and Drives (PEMD2022) (IET, 2022), 260–265.

30. P. Dowell, "Effects of Eddy Currents in Transformer Windings," *Proceedings of the Institution of Electrical Engineers* 113, no. 8 (1966): 1387–1394.

31. B. Li, Q. Li, and F. C. Lee, "A Novel PCB Winding Transformer With Controllable Leakage Integration for a 6.6 kW 500 kHz High Efficiency High Density Bi-Directional On-Board Charger," in 2017 IEEE Applied Power Electronics Conference and Exposition (APEC) (IEEE, 2017), 2917–2924.

32. M. D'Antonio, S. Chakraborty, and A. Khaligh, "Planar Transformer With Asymmetric Integrated Leakage Inductance Using Horizontal Air Gap," *IEEE Transactions on Power Electronics* 36, no. 12 (2021): 14014–14028.

33. L. Wu, L. Xiao, J. Zhao, and G. Chen, "Modelling and Optimisation of Planar Matrix Transformer for High Frequency Regulated LLC Converter," *IET Power Electronics* 13, no. 3 (2020): 516–524.

34. A. Taylor, J. Lu, L. Zhu, K. H. Bai, M. McAmmond, and A. Brown, "Comparison of SiC MOSFET-Based and GaN HEMT-Based High-Efficiency High-Power-Density 7.2 kW EV Battery Chargers," *IET Power Electronics* 11, no. 11 (2018): 1849–1857.

35. Magnetics Ferrite Catalog (2013), https://www.mag-inc.com/Media/Magnetics/File-Library/Product%20Literature/Ferrite%20Literature/Magnetics2013FerriteCatalog.pdf.

36. D. Han, C. T. Morris, W. Lee, and B. Sarlioglu, "A Case Study on Common Mode Electromagnetic Interference Characteristics of GaN HEMT and Si MOSFET Power Converters for EV/HEVs," *IEEE Transactions on Transportation Electrification* 3, no. 1 (2016): 168–179.